Ridged Meandered Waveguides for 3-D Routing and Phase Delay Control and Its Application to Discrete Lenses

Lisa Berretti, Renaud Loison, Esteban Menargues, Santiago Capdevila, Lucas Polo-López, Giovanni Toso, María García-Vigueras

Ridged Meandered Waveguides for 3D Routing and Phase Delay Control and its application to Discrete Lenses

Lisa Berretti, *Member, IEEE,* Renaud Loison, Esteban Menargues, Santiago Capdevila, Lucas Polo-López, *Senior Member, IEEE,* Giovanni Toso, *Fellow, IEEE,* María García-Vigueras, *Member, IEEE*

***Abstract*—In this paper, an innovative procedure to design ridged meandered waveguides is introduced. By modulating the meandered centerline of a waveguide connecting two fixed points, new degrees of freedom to control the phase delay are obtained. Ridged meandered waveguides represent a good compromise between coaxial cables, which feature broadband operation and can be easily bended still introducing high losses and conventional waveguides, which are characterized by low losses but also narrow operational bandwidth. Ridged meandered waveguides are especially well-suited for isophase lattice expanders that can be used in beamforming networks, phased arrays or discrete 3D lens antennas. The article describes a methodology to design meandered waveguides, which is verified both analytically and experimentally through the synthesis, fabrication and test of a discrete 3D lens antenna in Ka-band (27.5-30 GHz) made using additive manufacturing.**

***Index Terms*—Additive manufacturing, beamforming networks, discrete lens, dual polarization, Ka-band, phase delay control, ridged meandered waveguide, 3D routing.**

I. Introduction

CONTROLLING phase delays of guided waves is essential in the design of radio-frequency (RF) systems requiring signal distribution, recombination or beamforming. Such functionality is implemented in a wide range of devices, spanning from simple components (such as turnstile orthomode transducers [1] or mode extractors [2]), to more complex distribution systems such as multiport amplifiers [3] or antenna beamforming networks (BFNs) [4], [5].

The control of the phase delay combined with spatial routing of the signals can become an important challenge. The typical accommodation constraints are related to the interconnection of profiles with different lattices, or to the need for some internal space to accommodate other devices for the control of active elements and/or for thermal dissipation management. In this context, routing mechanisms providing high flexibility are typically desired [6]–[8].

The most frequent solution for the RF signals routing is based on the use of transmission lines implemented in a printed circuit board (PCB) layout (microstrip and stripline, among others), as in [9], [10]. This configuration is chosen for its low cost and high suitability for integration of active electronic components. Still, this solution is very limited for 3D routing, it has significant insertion losses and is only applicable in low-power systems. Coaxial cables are an alternative to PCB routing since they allow interconnections with complex 3D trajectories [11], [12]. However, their insertion losses are not negligible and high-power handling is an issue.

Conventional waveguides allow for signal routing with very low insertion losses and high-power handling [13]–[16]. Yet, their fabrication is very cumbersome, since it involves the assembly of discrete waveguide parts (including bends, twists, etc), which might lead to practical performance issues due to imperfect assembly. Substrate integrated waveguide (SIW) and the recent air-filled version (AF-SIW), appear as a compromise between waveguide and PCB technology, offering medium loss and low cost, [17], [18]. High-power handling and 3D routing are still an issue in these two technologies.

In this context, additive manufacturing (AM) appears as an enabling solution to conceive routing networks that combine low insertion losses, high-power handling, extreme flexibility and low cost [19]–[21]. Fully metallic meandered waveguides (MW) have been recently proposed in [7] to synthesize desired phase delays between two assigned points. The resulting complex curvatures can only be fabricated in AM technology. Indeed, such technology enables monolithic pieces or even monolithic clusters, thus simplifying problems associated to assembly.

Ridged meandered waveguides (RMW) represent a step further in MWs, since they entail an enhancement of the bandwidth. In fact, they present an interesting middle point between the non-dispersive TEM propagation of coaxial cables and the narrow bandwidth of conventional waveguides.

The objective of this paper is to propose an analytical procedure to synthesize arbitrary and broadband phase delays using RMWs, in order to enable fully-metallic systems for space applications. The procedure is demonstrated through the design and manufacturing of a RMW-based three-dimensional discrete lens.

The paper is organized as follows: Section II presents the analytical description of the RMW trajectory connecting two points allowing the building of the path, the phase delay synthesis and the dual-ridge cross-section evolution. In Section III the application of a RMW cluster in a 3D discrete lens antenna is proposed. Finally, in Section IV, an experimental

L. Berretti, R. Loison, L. Polo-López, and M. García-Vigueras are with the Institut d'Electronique et des Technologies du numeRique (IETR), UMR CNRS 6164, INSA Rennes, Rennes, France (e-mail: lisa.berretti@insa-rennes.fr).

E. Menargues, and S. Capdevila are with SWISSto12, Renens, Switzerland.

G. Toso is with Radio Frequency Payloads and Technology Division, European Space Research and Technology Centre (ESTEC), European Space Agency (ESA), 2200AG Noordwijk, The Netherlands.

This article has been accepted for publication in IEEE Transactions on Antennas and Propagation. This is the author's version which has not been fully edited and content may change prior to final publication. Citation information: DOI 10.1109/TAP.2023.3255515

validation of the proposed concept is presented through the manufacturing and the measurement of a 3D discrete lens prototype.

II. Design of Ridged Meandered Waveguides

MWs can be defined as waveguides with a modulated profile along the propagation axis. RMWs are MWs whose cross-section corresponds to a ridged waveguide. The goal is to design RMW able to connect two assigned points (indicated as starting and ending points P_s and P_e) through a tailored trajectory that guarantees a desired phase delay.

To design a MW or RMW, two waveguide ports placed in the starting and ending points should be connected. The following hypothesis are considered (as displayed in Fig. 1):

- the two waveguide ports have the same cross-section, which is maintained throughout the trajectory;
- the waveguide ports centered in the starting and ending points are parallel to the xy plane;
- the profile followed by the RMW should be characterized by a function continuous and with a continuous first derivative.

The problem is split into four sub-problems: the design of the RMW centerline or trajectory connecting the two points, the design of the waveguide along the trajectory, the design of the waveguide cross-section and the phase delay synthesis.

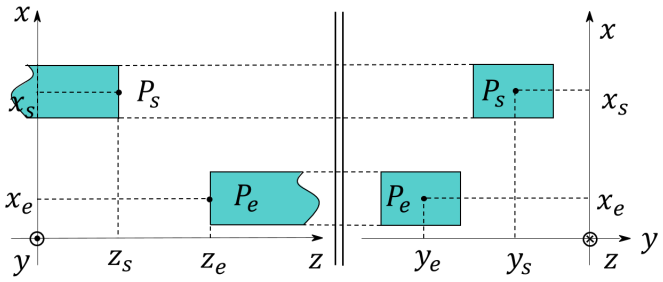

Fig. 1: Waveguide connection specifications.

A. MW trajectory

To build the MW baseline trajectory, an auxiliary axis t that connects the points P_s (where $t = 0$) and P_e (where $t = 1$) is considered (see Fig. 2).

The 3D trajectory path curve $P(t)$ starts at P_s and ends at P_e:

$$\begin{cases} P(0) = P_s \\ P(1) = P_e \end{cases} \tag{1}$$

and it is built in such way to enable an arbitrary modulation of the phase delay. The curve should be perpendicular to the xy plane at $t = 0$ and $t = 1$ to ensure differentiability at the connection points.

To reach these goals, the MW trajectory is defined as follows:

$$\vec{OP}(t) = \vec{OP}_s(t) + \vec{b}(t) + \vec{m}(t) \tag{2}$$

being $\vec{b}(t)$ a baseline function to properly connect P_s and P_e and $\vec{m}(t)$ a modulating function to synthesize the phase delay. To satisfy Eq. (1), the following relations are verified:

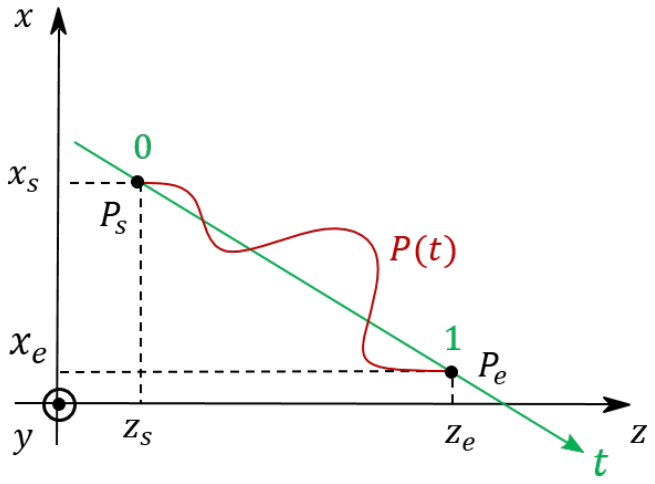

Fig. 2: Trajectory path curve $P(t)$ between the starting and ending points defined in t coordinate system in xz plane.

$$\begin{cases} \vec{b}(0) = \vec{0} \\ \vec{b}(1) = \vec{P_sP_e} \\ \vec{m}(0) = \vec{0} \\ \vec{m}(1) = \vec{0} \end{cases} \tag{3}$$

In order to ensure differentiability in the connection points, some conditions on the derivative functions are included:

$$\begin{cases} \frac{d\vec{b}}{dt}(0) \text{ and } \frac{d\vec{b}}{dt}(1) \text{ both oriented along } \hat{z} \\ \\ \frac{d\vec{m}}{dt}(0) \text{ and } \frac{d\vec{m}}{dt}(1) = \vec{0} \end{cases} \tag{4}$$

Thus, the baseline is defined as follows:

$$\vec{b}(t) = (x_e - x_s)s(t)\hat{x} + (y_e - y_s)s(t)\hat{y} + (z_e - z_s)t\hat{z} \tag{5}$$

being $s(t)$ the step function defined employing the formulation proposed in [22]:

$$s(t) = \frac{1}{\beta w}\ln\left(\frac{1 + e^{\beta(t-t_0+w/2)}}{1 + e^{\beta(t-t_0-w/2)}}\right), \quad t \in [0, 1] \tag{6}$$

where t_0 defines the inflection point of the step function while w and β are the slope parameters (Fig 3). These parameters can be used as degrees of freedom, giving flexibility in the design of MW. To verify the conditions of continuity and derivability (Eq. (3) and (4)), the following conditions are determined experimentally: $\beta w \geq 11$ for $t_0 = 0.5$, while $\beta w \geq 22$ for $t_0 = 0.4$ or 0.6, as shown in Fig 3.

To synthesize different phase delays, a modulating function is added:

$$\vec{m}(t) = m(t)\vec{e}_m \tag{7}$$

where $\vec{e}_m = \delta\hat{x} + \gamma\hat{y}$ is a unit vector defining the modulation plane that can be freely chosen while $m(t)$ is given by:

$$m(t) = A\sin(\pi P t)\sin^2(\pi t) \tag{8}$$

The amplitude A and semi-periods P are degrees of freedom that allow to control the trajectory length and the phase delay, as discussed in [7] and displayed in Fig. 4.

This article has been accepted for publication in IEEE Transactions on Antennas and Propagation. This is the author's version which has not been fully edited and content may change prior to final publication. Citation information: DOI 10.1109/TAP.2023.3255515

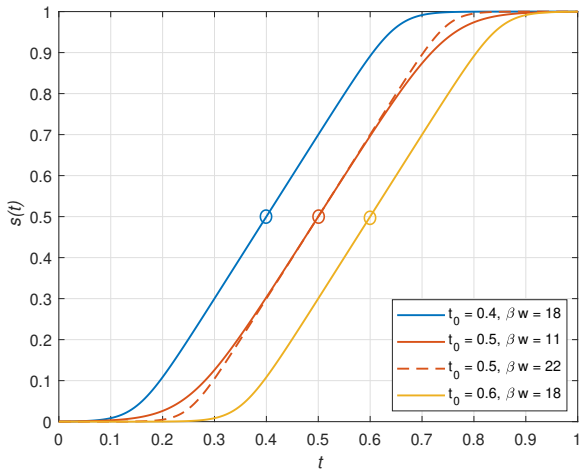

Fig. 3: Examples of step functions varying t_0 and the product βw.

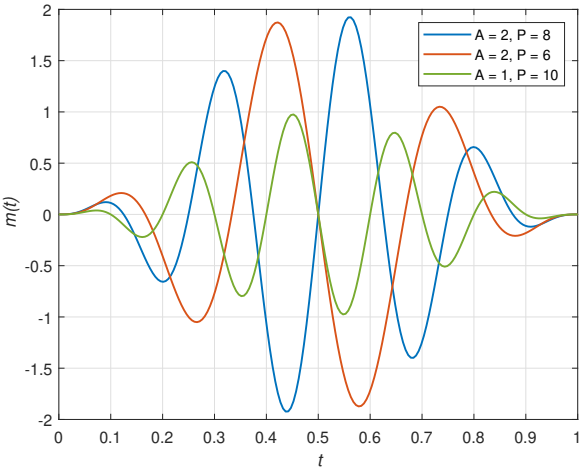

Fig. 4: Modulation function $m(t)$ for different modulation parameters (A and P).

B. Cross-section transport approach

In order to build accurately RMWs, a smooth evolution of the RMW cross section along the trajectory $\vec{OP}(t)$, based on the *parallel transport approach* [23]–[25], is implemented. Through this algorithm, an orthonormal basis of vectors ($\vec{n}$, $\vec{u}$, $\vec{v}$) is constructed along the modulated centerline from the starting to the ending point, as displayed in Fig. 5. The implemented basic steps of the parallel transport algorithm for piece-wise linear curves are here defined.

The unit vector perpendicular to the cross-section (and tangential to the trajectory) is described by:

$$\vec{n}_{i+1} = \frac{\vec{OP}_{i+1} - \vec{OP}_i}{||\vec{OP}_{i+1} - \vec{OP}_i||}, \quad i = 0, .., N-2 \qquad (9)$$

where $\vec{OP}_i = \vec{OP}(t_i)$, $\vec{n}_i = \vec{n}(t_i)$ with $t_i = i/N$. At the extreme points of the trajectory, the tangential vector must be parallel to the z-axis: $\vec{n}_o = \vec{n}_N = \hat{z}$.

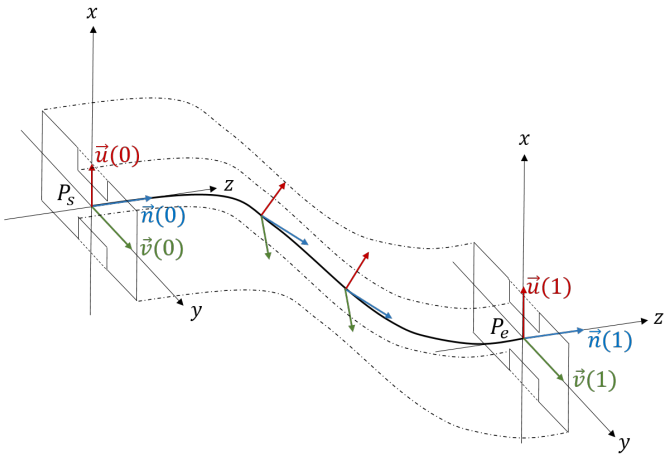

Fig. 5: Orthonormal basis ($\vec{n}(t)$, $\vec{u}(t)$, $\vec{v}(t)$) along a centerline connecting starting and ending points.

The vector $\vec{u}$, perpendicular to the modulated centerline, is implemented starting from an initial orientation $\vec{u_0}$ (vector that defines the orientation of the waveguide cross-section at the starting point) as follows:

$$\vec{u}_{i+1} = R(\vec{B}_{i+1}, \theta_{i+1})\vec{u}_i, \quad i = 0, .., N-1 \qquad (10)$$

being the vector $\vec{B}_{i+1} = \frac{\vec{n}_i \times \vec{n}_{i+1}}{||\vec{n}_i \times \vec{n}_{i+1}||}$ and the evaluated angle $\theta_{i+1} = \arccos(\vec{n}_i \cdot \vec{n}_{i+1})$, $R(\vec{B}, \theta)$, the rotation matrix by the angle θ about the vector $\vec{B}$.

The third vector is expressed by the cross product of the already defined vectors: $\vec{v}_i = \vec{n}_i \times \vec{u}_i$. Such vectors form an orthonormal basis in each point of the discretized trajectory to define the RMW cross-section evolution along it. In Fig. 5, the RMW is implemented by simply repeating the waveguide cross-section along the modulated curve.

C. RMW cross-section

The previous synthesis method can be applied to any type of waveguide cross-section. In our case, the RMW is implemented considering a dual-ridge waveguide defined in Fig. 6.

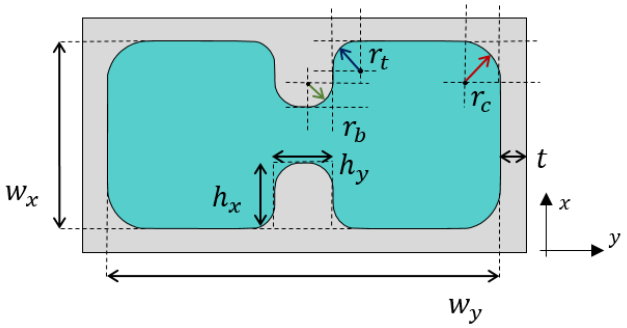

Fig. 6: Ridged rectangular waveguide cross-section with $h_x = 1$ mm, $h_y = 1$ mm, $w_x = 3$ mm, $w_y = 7$ mm, $r_t = 1$ mm, $r_b = 1$ mm, $r_c = 1.5$ mm and $t = 0.25$ mm.

The ridges allow to increase the single-mode bandwidth of the waveguide since they lower the cutoff frequency of the

This article has been accepted for publication in IEEE Transactions on Antennas and Propagation. This is the author's version which has not been fully edited and content may change prior to final publication. Citation information: DOI 10.1109/TAP.2023.3255515

fundamental mode. In Fig. 7, four waveguides with different cross-sections are considered. When decreasing the cut-off frequency of the fundamental mode, the propagation constant vs frequency becomes more linear around a selected operation frequency, as 28.5 GHz in this paper. It must be highlighted that, the flatter the line, the closer to true-time delay and a broadband operation. It is interesting to notice the difference between the black curve (empty waveguide) and the blue curve (ridge waveguide), and how the ridge waveguide enables low loss, wave guiding with minor influence of the dispersion inherent to waveguides.

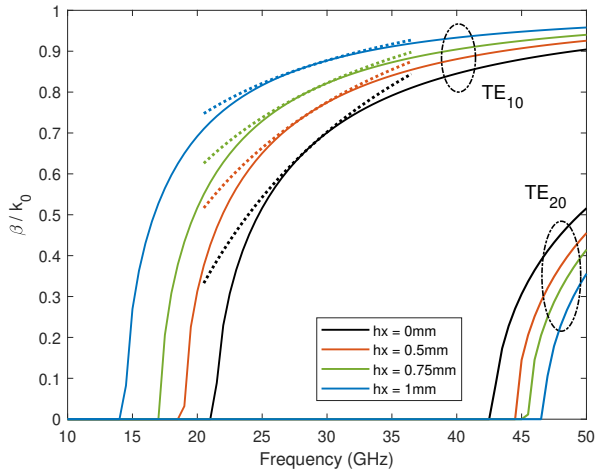

Fig. 7: Dispersion curves of rectangular and dual-ridge waveguides for the two first propagating modes (TE_{10}, TE_{20}).

D. RMW synthesis and optimization

The flexibility of the proposed method to build RMWs consists in connecting two arbitrary points and playing on some design parameters of the modulated curves, to properly match the specifications on the phase and amplitude. In Fig. 8 some examples of RMWs are depicted. In particular, Fig. 8a shows a simple step function with a displacement in the x and z coordinates, while Fig. 8b to Fig. 8d show RMWs with exotic meanderings with several displacements in coordinates.

When connecting two points, a desired phase delay can be obtained with several design parameter combinations. As an example, Fig. 9 shows the semi-period P as a function of the amplitude modulation A that leads to a specific RMW physical centerline length. Obviously, strong curvatures will induce reactive effects that affect the RMW physical centerline length synthesis and should be avoided (these cases correspond to extreme values of A and P). If possible, intermediate values of A and P are recommended to bypass the mismatching between RMW electrical and physical lengths. It is important to note that it is not possible to derive with a single analytical equation the couple of perfect values for A and P, since reactive effects could not be easily predicted and also the position of the connecting points are playing an important role. The choice of A and P is also made by considering the available space to accommodate the RMW and its physical manufacturability. A design recommendation is to use a separation between the two points such that the bends that appear along the centerline exhibit a bending radius larger than the height of the waveguide cross-section. This design recommendation will produce bends in the centerline that are smooth and do not cause reactive effects that affect the insertion phase. The RMW design process starts by defining the step function. In order to avoid discontinuities at the connection points and sharp slopes, the inflection point is fixed in the center $t_0 = 0.5$ while the recommendation for inclination parameters is $\beta w = 11$ with $\beta = 22$ and $w = 0.5$. A and P are chosen and optimized to reach the desired phase delay. Such phase delay in the RMW is computed as $\Phi_{wg} = \beta_{wg} L_{wg}$, where β_{wg} is the waveguide propagation constant and L_{wg} is the physical length of the centerline. To synthesize a given delay, the designer can adjust both L_{wg} (through A and P) and β_{wg} (through the cutoff frequency of the fundamental mode in the RMW, by adjusting the cross-section dimensions). For cluster design, the recommendation is to define physically feasible starting points and optimize from there using any optimization routine that minimizes globally the difference between the synthesized delay and the desired one.

III. Application of RMW to Spaceborne 3D Discrete Lens Antennas

In this section, the versatility and high potential of the RMW synthesis are illustrated through the application case of a 3D discrete lens in Ka-band for telecommunication applications.

A. Basics of 3D discrete lens antennas

Three-dimensional (3D) discrete lens antennas have been extensively studied in the open literature. In particular, in [26]–[28], the results of recent investigations on their properties, number of Degrees of Freedom (DoF), focal points (or foci) and optical aberrations are presented.

In this paper, a 3D discrete lens antenna configuration with 3 perfect focal points or DoF is considered (introduced in [27]). The simple sketch in Fig. 10 illustrates the main structure of a 3D discrete lens, which is mainly constituted by:

- the focal arc containing the foci, whose positions are defined by azimuth and elevation input angles (θ_{in}, ϕ_{in});
- the back array profile of coordinates $(X_{back}, Y_{back}, Z_{back})$;
- the front array profile of coordinates $(X_{front}, Y_{front}, Z_{front})$;
- the grey box representing the part of the lens that implements the delay W induced between the back and front profiles.

This paper considers the possibility to introduce a magnification factor M, which is defined as:

$$\sin(\theta_{out}) = M \sin(\theta_{in}) \tag{11}$$

In this paper, the value of M is chosen smaller than 1, which can be see as a zooming capability, since it implies that $\theta_{in} > \theta_{out}$ (as shown in Fig. 10). This capability provides a certain freedom to control the positioning of the sources in the focal arc (related to θ_{in}) with respect to the pointing angle of the

This article has been accepted for publication in IEEE Transactions on Antennas and Propagation. This is the author's version which has not been fully edited and content may change prior to final publication. Citation information: DOI 10.1109/TAP.2023.3255515

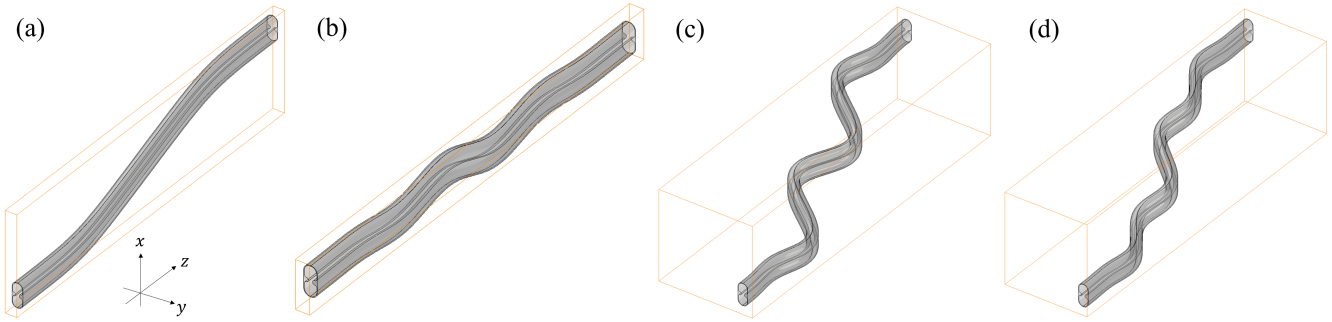

Fig. 8: Examples of ridged meandered waveguides with different cuvatures between two points $P_s(x_o, y_o, z_o)$ and $P_e(x_o+\Delta_x, y_o+\Delta_y, z_o+\Delta_z)$: (a) step function with displacement $\Delta_x = 2\lambda, \Delta_y = 0, \Delta_z = 10\lambda$, (b) meandering in the E-plane with $A = 2$, $P = 8$ and displacement $\Delta_x = 0, \Delta_y = 0, \Delta_z = 10\lambda$, (c) meandering in the E-plane with $A = 12$, $P = 8$ and displacement $\Delta_x = 2\lambda, \Delta_y = 4\lambda, \Delta_z = 10\lambda$, (d) meandering in the E-plane with $A = 8$, $P = 6$ and displacement $\Delta_x = 2\lambda, \Delta_y = 2\lambda, \Delta_z = 10\lambda$.

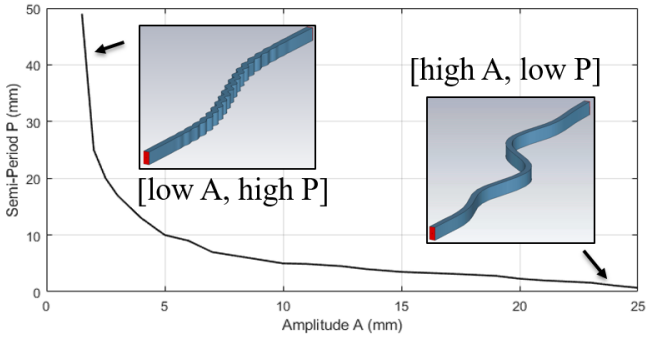

Fig. 9: Semi-periods vs amplitude modulation parameters for a specific length to synthesize.

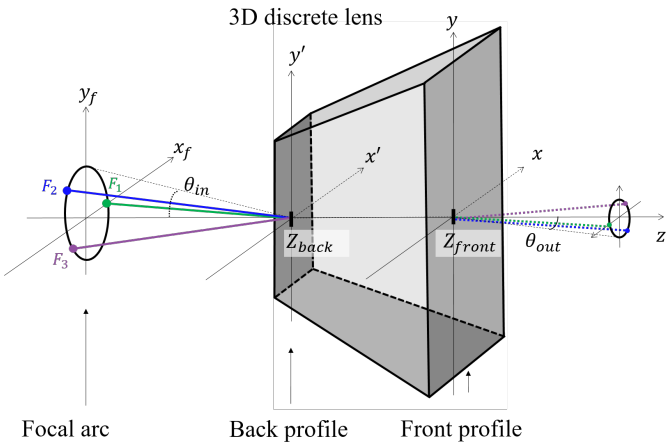

Fig. 10: Sketch of a 3D discrete lens with flat back and front profiles ($Z_{front} = 0$ and $Z_{back} = -\Delta_z$). The considered configuration has three perfect focal points and implements a zooming factor $M < 1$. The grey box represents the core of the 3D lens, where the phase delays W between the front and back profiles is implemented.

beam that they generate (related to θ_{out}). It is worth noting that this type of zooming capability, or magnifying effects, are valid for reflector antennas [29], [30] as well as for lens antennas [26]–[28].

As it is explained in [31], the number of perfect foci in 3D discrete lenses is determined by its number of degrees of freedom. This manuscript proposes to implement 3 perfect foci, as shown in Fig. 10, in order to define a focal arc where multiple sources will be placed in order to attain multibeam operation. In general, the variables required to define a 3D discrete lens are 7: the coordinates X_{back}, Y_{back}, Z_{back}, X_{front}, Y_{front}, Z_{front} and phase delays W.

After fixing a priori two of the seven variables of the lens, i.e. flat back and front profiles ($Z_{front} = 0$, $Z_{back} = -\Delta_z$) and choosing other two variables (X_{back}, Y_{back}) as independent variables, the remaining variables in the lens are: the coordinates of the elements in the front profile (X_{front}, Y_{front}) and the delay W. This allows to synthesize 3 perfect foci [27]. As a conclusion, in order to implement 3 foci, the lattice in the front profile will not be regular. The complete formulation can be found in [27].

The three foci are distributed in a circle perpendicular to the axis of the lens at azimuth angles equal to ϕ_{in} = [0, 120, 240]°. The three foci are represented by the points F_1, F_2 and F_3 in Fig. 10.

B. 3D discrete lens antenna using RMW for space-borne applications

As potential application case, the design of a multibeam antenna for geostationary (GEO) satellites is considered. GEO antennas have a field of view limited to ±8°, so grating lobes (GL) appearing at angles outside of this range are acceptable [32]. Thus, this application imposes the maximum pointing angle required in the lens antenna of $\theta_{out} = 8°$.

For this application example, a Ka-band receive (RX) antenna is selected, whose center frequency is $f_0 = 28.5$ GHz. Dual circular polarization shall be supported. Other design choices are: rectangular lattice for the front and back profiles and periodicity in the front array around 3λ, (typical choice for GEO active antennas to avoid GLs within the field of view ±8°). A magnification factor of $M = 0.5$ enables a relaxed feed cluster design and accommodation with input

This article has been accepted for publication in IEEE Transactions on Antennas and Propagation. This is the author's version which has not been fully edited and content may change prior to final publication. Citation information: DOI 10.1109/TAP.2023.3255515

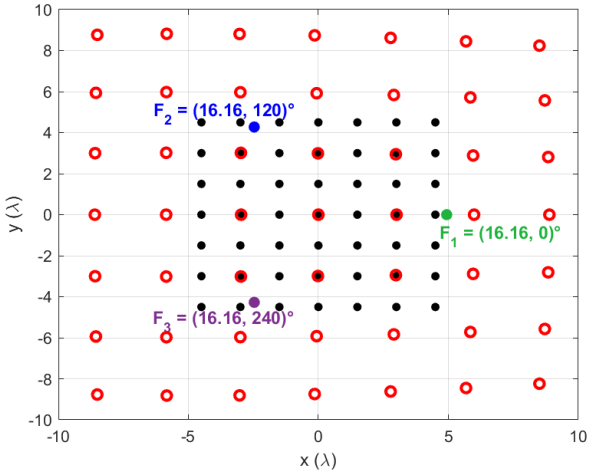

Fig. 11: Bi-dimensional projection of 7x7 square 3D discrete lens antenna with assigned back profile (black dots), front profile (red circles) and 3 perfect foci F_1, F_2 and F_3 (with $M = 0.5$, $f/D_{back} \approx 2$).

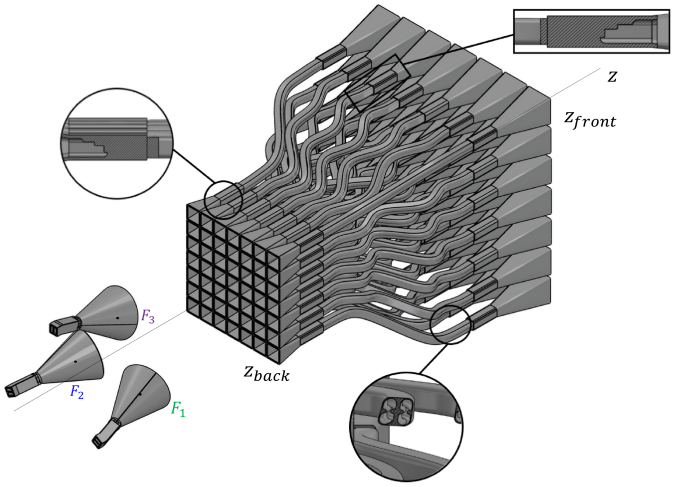

Fig. 12: 7x7 CST model of the 3D discrete lens antenna design including the RMW cluster with $f/D_{back} \simeq 2$, feeds placed in the 3 perfect evaluated foci with an azimuth angle θ_{in} = 16.16° and elevation angle ϕ_{in} = [0, 120, 240]°.

angle $\theta_{in} = 16.16°$, while closer elements in the back profile with a periodicity of 1.5λ. The back profile is assigned a priori in its coordinates to perfectly fit the back periodicity (being the one smaller), while the coordinates of the front lens aperture are derived from the Geometrical Optics equations in [27].

Despite the final antenna will have several hundreds of radiating elements, the example included in this article is restricted to $N_e = 49$ (7×7 elements per side of the lens) to reduce the computational effort of the full-wave simulations. The transversal cross sections of the front and back profiles of the considered 7×7 lens are shown in Fig. 11, considering the assigned back profile with black dots, the dependent front profile with red circles and the three perfect foci. It can be noticed again that the elements in the back profile follow a regular lattice, whereas the ones in the front profile are placed in an irregular one.

The CST model of the $7 \times 7-$element lens is shown in Fig. 12. It consists on the following parts:

- a feed cluster with dual circular polarized horns, each one backed by a septum polarizer to produce the circular polarization;
- the back-side array, which is formed by 7×7 square 1.5λ horns (each horn is backed by a septum polarizer and connected to a pair of RMW);
- the front-side array, which is formed by 7×7 square 3λ horns (each horn is backed by a septum polarizer and connected to a pair of RMW);
- the cluster of RMW, which connects the back array to the front one.

It must be noticed that each element in the lens has two side-by-side RMWs, one per polarization. Indeed, in real operation, a beam or signal is received by all the horns in the front array, each one receiving a portion of the complete circularly-polarized signal. The signals received by each front-side horn is transformed from circular to linear by the septum polarizer; depending on the polarization, they will travel through the

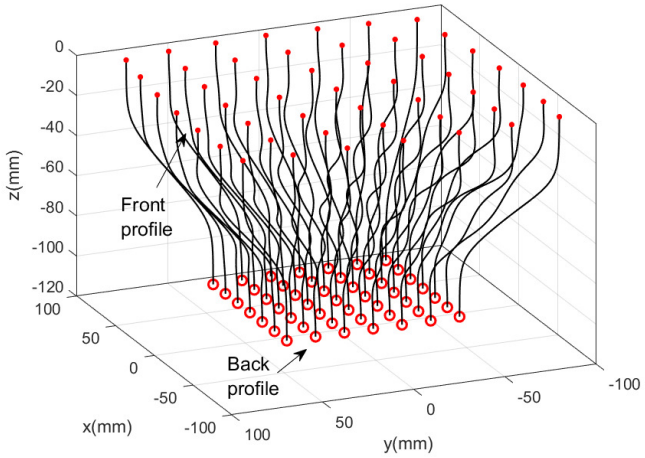

Fig. 13: Cluster of $\vec{OP}(t)$ RMW trajectory (black curves with curvature for each element) connecting back (red circles) and front profile (red points) with vertical height of $\Delta_z = 13\lambda$.

right-handed RMWs or through the left-handed RMWs. After the RMWs, the septum polarizers in the back-side horns transforms again the linear polarization into a circular one. The signals then travel through the free-space between the back array and the feed cluster, where circularly-polarized feeds connected to rest of the payload finally receive the signal.

C. Synthesis of RMW cluster

In order to synthesize the phase delays of the RMW cluster of the lens, additional considerations to ensure the system physical feasibility must be considered. In particular, one must pay attention to avoid the collision between neighbour RMW for a pair of given lattices by carefully considering the height between profiles, the modulation planes, and the step and modulation parameters, as it has been anticipated in Section

II D. For the example in this article, the choices are only E-plane modulated waveguides ($\delta = 0$, $\gamma = 1$), and a RMW cluster height, Δ_z, equal to 13λ. In order to design the lens antenna, a RWM cluster that produces delays (Φ_{wg}) that are as close as possible to the ideal ones, $\Phi_{des} = k_0 W$ should be derived. The resulting cluster of centerlines after optimization is shown in Fig. 13. The associated amplitudes, A, and semi-periods, P, to produce the required phase delays using RMWs are presented in Table I and II.

TABLE I: Matrix of amplitude parameters A's for the 7x7 RMWs cluster.

0.00	11.31	10.38	10.18	10.02	9.32	4.30
−8.54	11.06	12.59	12.85	12.99	11.16	−8.54
10.62	13.28	13.98	13.68	13.51	13.07	10.12
11.83	14.05	14.54	14.56	14.16	12.02	9.21
10.62	13.28	13.98	13.68	13.51	13.07	10.12
−8.54	11.06	12.59	12.85	12.99	11.16	−8.54
0.00	11.31	10.38	10.18	10.02	9.32	4.30

TABLE II: Matrix of semi-periods parameters P's for the 7x7 RMWs cluster.

0.00	3.90	5.00	5.52	5.40	4.94	3.90
−5.46	5.62	5.29	5.57	5.32	5.51	−5.38
5.71	5.38	5.61	5.87	5.73	5.38	5.52
5.30	5.30	5.60	5.70	5.66	6.01	6.30
5.71	5.38	5.61	5.87	5.73	5.38	5.52
−5.46	5.62	5.29	5.57	5.32	5.51	−5.38
0.00	3.90	5.00	5.52	5.40	4.94	3.90

D. Results

This sub-section reports the numerical results characterizing the 7×7 discrete lens antenna shown in Fig. 12. First of all, the antenna is analysed using house-made geometrical optics tools implemented in MATLAB. In addition, full-wave simulations using CST Microwave Study are considered.

The computed MATLAB patterns for the three perfect foci are displayed in Fig. 14 with respect to the conventional *uv* coordinates. As expected, the main beams are pointing at $\theta_{out} = 8^\circ$ and the three azimuthal angles coincide with the ones of the homologous focal points. The grating lobes are outside of the field of view (red circle in Fig. 14), as required in a GEO antenna.

Concerning the CST simulation, the feed horns are placed in the perfect foci positions and have a peak directivity of $D_f = 21$ dBi. The size of such horns has been chosen to provide an edge-tapering illumination of about -10 dB in the back profile considering the ratio $f/D_{back} = 1.9895$. Secondly, concerning the back-side of the lens, the size of the corresponding squared horns is determined in order to fill the available space. For this reason, horns with an edge length of 1.35λ are chosen, providing a peak directivity of $D_b = 7.4$ dBi. On the front-side, square horns with side of 2.32λ are selected, which provide a maximum directivity of 17.5 dBi. It must be highlighted that the horns do not fully fill the available space, but the selected size permits to have horns that have some space in between, required later for assembly using a screwdriver.

Fig. 15 compares the numerical results obtained with Geometrical Optics and the full-wave simulation by CST, considering the feed placed in the perfect focal point F_1 ($\theta_{in} = 16.16^\circ$, ϕ_{in} = 0°). Identical results are obtained for the other two foci. The resulting beam is pointing at ($\theta_{out} = -8^\circ$), as expected. Both analysis methods agree very well, which validates the RMW synthesis methodology and its implementation using CST.

IV. Experimental validation

For the experimental validation, a representative but reduced prototype (size: 3×3) is proposed. It must be highlighted that the goal of this activity is to validate the RMW through comparison between measurements and simulations. Fig. 16 and Fig. 17 show the cluster of RMW and the CST model of the complete device used for the exercise, which maintains the dual-polarization feature and zooming factor ($M = 0.5$) of the previous antenna, as well as the f/D_{back} ratio, input and output pointing angles. The number of feeds is 7: $3\times$ at the perfect foci ϕ_{in} = [0, 120, 240]°, $3\times$ at mirrored angles ϕ_{in} = [60, 180, 300]°, and $1\times$ at boresight direction.

The fabricated prototype is shown in Fig. 18. AM using raw Aluminium finish is used to produce the RF functional part (antennas, feeds, cluster of RMW) while conventional machining is used to fabricate the fixture that holds all parts together. The prototype consists in the following parts:

- $1\times$ monolithic part that includes the RMW cluster and the back septum-horns, which is 3D printed vertically to preserve the symmetries of the structure and ensure that the phase delays will be reproduced in the best possible way;
- $9\times$ standalone monolithic front septum-horns (note that the arrangement of horns in the front array is not purely periodic, as it was explained in Section III.A);
- $1\times$ monolithic $7-$feed cluster, and a separate $2-$waveguide expander to connect the coaxial to waveguide transitions;
- multiple Aluminum plates and bars to build and support the assembly feed + lens. Once assembled, these bars and plates are covered with absorbers.

In Fig. 19 and 20 numerical and experimental results are compared when the lens is illuminated by feeds placed in perfect foci ($\phi_{in} = 0^\circ$ and $\phi_{in} = 120^\circ$, respectively). The patterns are plotted in cut-planes corresponding to the specific azimuth angle. It is worth highlighting the good agreement between the co-polarized simulated and measured patterns, which experimentally validates the design of the RMW cluster. The cross-polarization measured is higher as compared to the simulated one, but still comparable to 20 dB, which might be caused by both the actual device but also spillover and setup reflections.

Finally, Fig. 21 shows the measured radiation patterns for a feed placed in a non-perfect focal point at both 27.5 GHz and 30 GHz. It is worth highlighting that the beam pointing remains stable at both frequencies, which proves

This article has been accepted for publication in IEEE Transactions on Antennas and Propagation. This is the author's version which has not been fully edited and content may change prior to final publication. Citation information: DOI 10.1109/TAP.2023.3255515

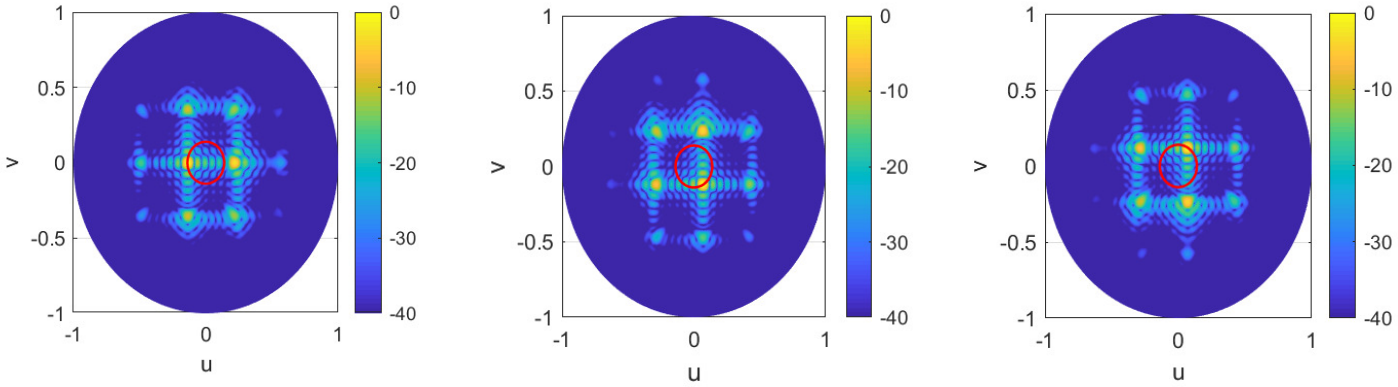

(a) (b) (c)

Fig. 14: Theoretical patterns in uv coordinates of the 7×7 lens antenna with feed placed in the three perfect foci ($\theta_{in} = 16.16°, \phi_{in} = [0, 120, 240]°$), with field of view $\pm 8°$ in red.

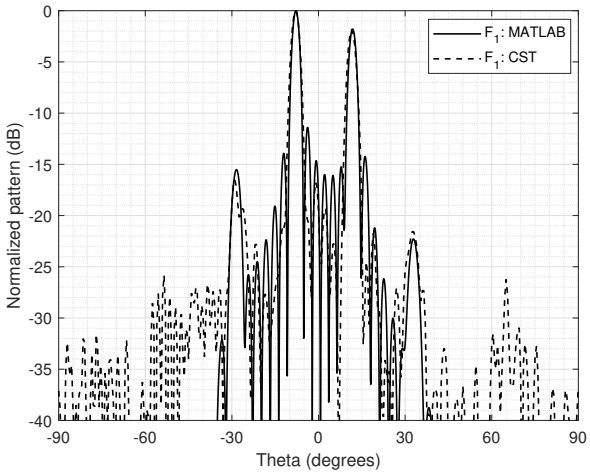

Fig. 15: Theoretical and simulated copolar pattern for the cut-plane $\phi_{cut} = 0°$ of the 7-by-7 discrete lens with the feed placed in the perfect focus position F_1 with ($\theta_{in} = 16.16°$, $\phi_{in} = 0°$).

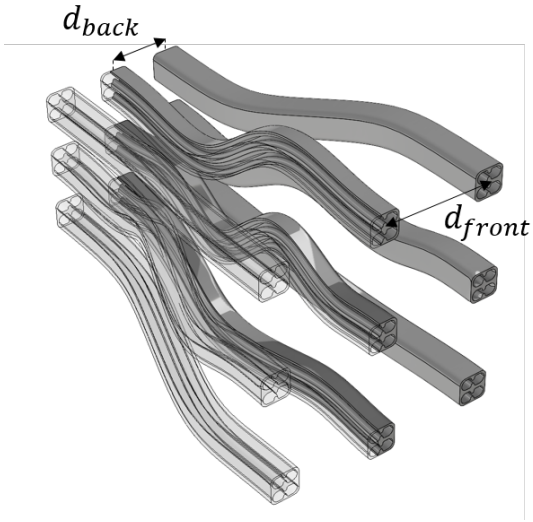

Fig. 16: 3×3 RMW cluster connecting back and front profiles with $d_{back} = 1.5\lambda$, $d_{front} \approx 3\lambda$, $\Delta_z = 10\lambda$.

the broadband characteristic of the RMW with respect to conventional waveguides. Finally, these measurements show that the beams point at $8°$ despite not being illuminated from a perfect focal point, which validates this lens antenna for multibeam applications.

V. Conclusion

The article has introduced an analytical methodology to design and control phase delays using RMW. RMWs permit to guarantee an accurate phase control over an increased frequency bandwidth as compared to conventional waveguides. The methodology also enables highly flexible 3D routing. The article validates this new technological solution through the design of two 3D discrete lens antennas (one with 7×7 elements, one with 3×3 elements), where the delays are implemented using RMWs. The 3×3 element lens is manufactured and measured results are in a very good agreement with the numerical ones. This study permits validating RMWs as

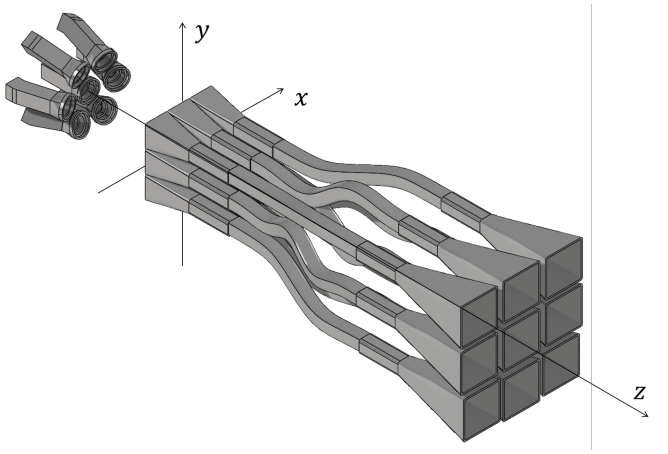

Fig. 17: CST model of 3×3 lens antenna with a cluster of 7 feed horns.

This article has been accepted for publication in IEEE Transactions on Antennas and Propagation. This is the author's version which has not been fully edited and content may change prior to final publication. Citation information: DOI 10.1109/TAP.2023.3255515

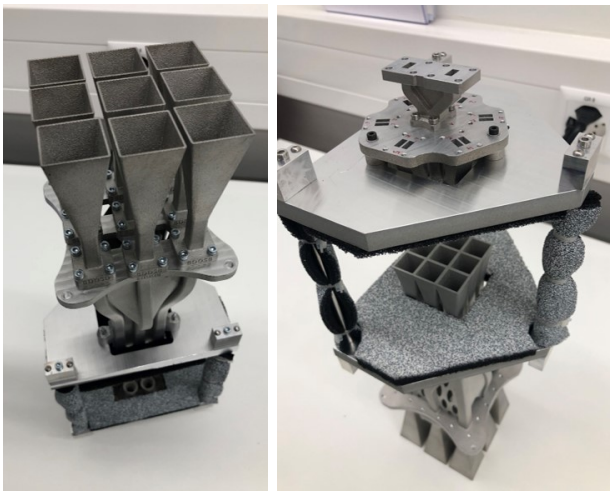

Fig. 18: Back and front view of the 3×3 lens manufactured by SWISSto12 using AM.

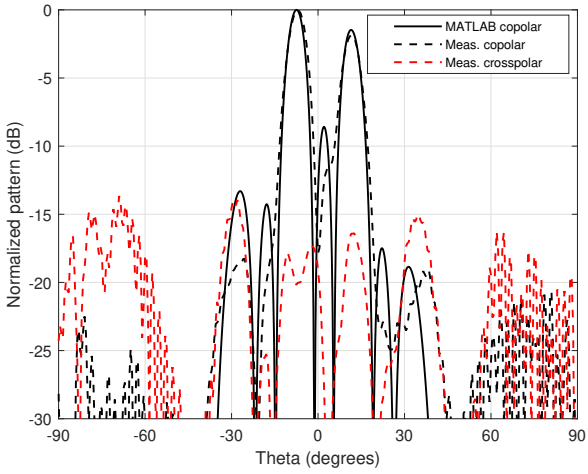

Fig. 19: Simulated and measured radiation patterns for the cut-plane $\phi_{cut} = 0^\circ$ of the 3×3 lens antenna; the active feed is placed in the perfect focal point ($\theta_{in} = 16.16^\circ$, $\phi_{in} = 0^\circ$); Co-polarization: RHCP, Cross-polarization: LHCP.

a promising and reliable solution for low-loss and broadband phase control.

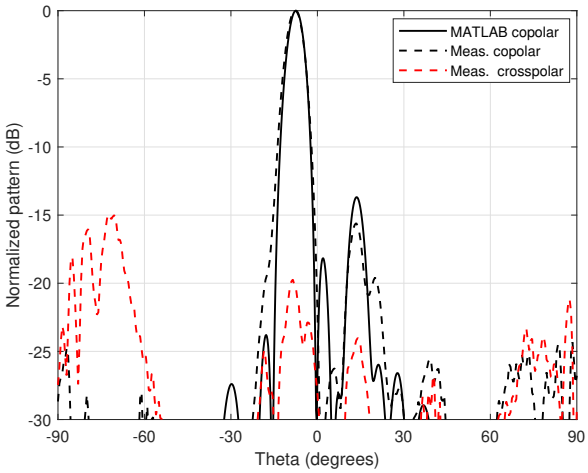

Fig. 20: Simulated and measured radiation patterns for the cut-plane $\phi_{cut} = 120^\circ$ of the 3×3 lens antenna; the active feed is placed in the perfect focal point ($\theta_{in} = 16.16^\circ$, $\phi_{in} = 120^\circ$); Co-polarization: RHCP, Cross-polarization: LHCP.

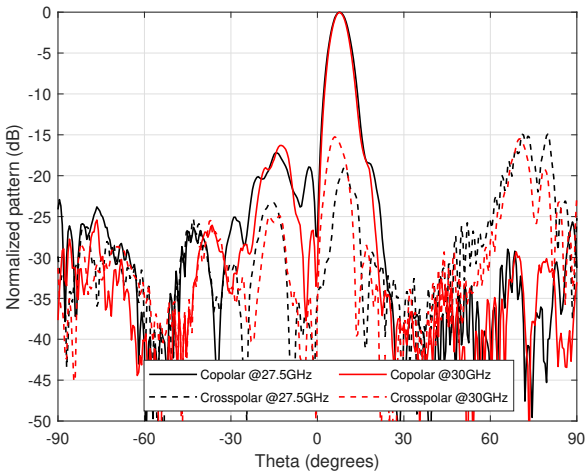

Fig. 21: Measured patterns at f = 27.5 and f = 30 GHz and for the cut-plane $\phi_{cut} = 240^\circ$ of the 3×3 lens antenna; the active feed is placed in the perfect focal point ($\theta_{in} = 16.16^\circ$, $\phi_{in} = 240^\circ$); Co-polarization: RHCP, Cross-polarization: LHCP

REFERENCES

[1] G. Pisano, L. Pietranera, K. Isaak, L. Piccirillo, B. Johnson, B. Maffei, and S. Melhuish, "A broadband WR10 turnstile junction orthomode transducer," *IEEE Microwave and Wireless Components Letters*, vol. 17, no. 4, pp. 286–288, 2007.

[2] A. K. Pandey, "Design of multimode tracking system for earth station antenna," in *2016 Asia-Pacific Microwave Conference (APMC)*, 2016, pp. 1–4.

[3] A. Mallet, A. Anakabe, J. Sombrin, and R. Rodriguez, "Multiport-amplifier-based architecture versus classical architecture for space telecommunication payloads," *IEEE Transactions on Microwave Theory and Techniques*, vol. 54, no. 12, pp. 4353–4361, 2006.

[4] A. B. Numan, J.-F. Frigon, and J.-J. Laurin, "Printed w -band multibeam antenna with luneburg lens-based beamforming network," *IEEE Transactions on Antennas and Propagation*, vol. 66, no. 10, pp. 5614–5619, 2018.

[5] M. Elmusrati and V. Hasu, "Random switched beamforming for uplink wireless sensor networks," in *2007 IEEE 65th Vehicular Technology Conference - VTC2007-Spring*, 2007, pp. 3150–3154.

[6] N. A. Sutton and D. S. Filipovic, "V-band monolithically integrated four-arm spiral antenna and beamforming network," in *Proceedings of the 2012 IEEE International Symposium on Antennas and Propagation*, 2012, pp. 1–2.

[7] E. Menargues, M. García-Vigueras, S. Capdevila, P. Angeletti, and G. Toso, "Meandered waveguides for active antennas," in *2021 15th European Conference on Antennas and Propagation (EuCAP)*, 2021, pp. 1–5.

[8] D. W. Woo, K. Oh, and D. K. Kong, "Hybrid waveguide feed network for aperiodic subarray beamforming," *IEEE Antennas and Wireless Propagation Letters*, pp. 1–5, 2022.

[9] K. Ding, X. Fang, Y. Wang, and A. Chen, "Printed dual-layer three-way directional coupler utilized as $3\times$ 3 beamforming network for orthogonal three-beam antenna array," *IEEE Antennas and Wireless Propagation Letters*, vol. 13, pp. 911–914, 2014.

[10] S.-K. Zhao, M. Lv, Z.-y. Zhang, Q. Chen, and G. Fu, "Planar two-dimensional scanning multibeam array antenna based on a 3×3 butler matrix network," *IEEE Antennas and Wireless Propagation Letters*, vol. 21, no. 6, pp. 1163–1167, 2022.

[11] A. Le Pera, I. Morris, G. Thomas, P. James, N. Wheatley, and P. Jung, "Novel spread spectrum approach to multi-port amplifier calibration," in *2014 7th Advanced Satellite Multimedia Systems Conference and the 13th Signal Processing for Space Communications Workshop (ASMS/SPSC)*, 2014, pp. 346–351.

[12] G. Ruggerini, P. G. Nicolaci, G. Toso, and P. Angeletti, "A Ka-band active aperiodic constrained lens antenna for multibeam applications: Active discrete lens antennas are promising alternative solutions for multibeam coverage using a single aperture," *IEEE Antennas and Propagation Magazine*, vol. 61, no. 5, pp. 60–68, 2019.

[13] C. Koenen, U. Siart, T. F. Eibert, G. D. Conway, and U. Stroth, "Design of a millimeter-wave phased array antenna for gaussian beam shaping and steering," in *2016 IEEE International Symposium on Phased Array Systems and Technology (PAST)*, 2016, pp. 1–4.

[14] N. J. G. Fonseca, S.-A. Gomanne, P. Castillo-Tapia, O. Quevedo-Teruel, T. Tomura, and J. Hirokawa, "Connecting networks for two-dimensional butler matrices generating a triangular lattice of beams," *IEEE Journal of Microwaves*, vol. 1, no. 2, pp. 646–658, 2021.

[15] Y. Quan, H. Wang, S. Tao, and J. Yang, "A double-layer multibeam antenna with 45° linear polarization based on gap waveguide technology," *IEEE Transactions on Antennas and Propagation*, vol. 70, no. 1, pp. 56–66, 2022.

[16] J. Fan, Z. Liu, J. Zhao, P. Zhen, H. Lu, Y. Liu, and X. Lv, "Millimeter-wave multimode beamforming network based on double-ridged waveguides," in *2021 International Conference on Microwave and Millimeter Wave Technology (ICMMT)*, 2021, pp. 1–3.

[17] J.-W. Lian, Y.-L. Ban, Q.-L. Yang, B. Fu, Z.-F. Yu, and L.-K. Sun, "Planar millimeter-wave 2-D beam-scanning multibeam array antenna fed by compact siw beam-forming network," *IEEE Transactions on Antennas and Propagation*, vol. 66, no. 3, pp. 1299–1310, 2018.

[18] I. Lima de Paula, S. Lemey, D. Bosman, Q. V. d. Brande, O. Caytan, J. Lambrecht, M. Cauwe, G. Torfs, and H. Rogier, "Cost-effective high-performance air-filled SIW antenna array for the global 5G 26 GHz and 28 GHz bands," *IEEE Antennas and Wireless Propagation Letters*, vol. 20, no. 2, pp. 194–198, 2021.

[19] A. Vafadar, F. Guzzomi, A. Rassau, and K. Hayward, "Advances in metal additive manufacturing: A review of common processes, industrial applications, and current challenges," *Applied Sciences*, vol. 11, no. 3, 2021. [Online]. Available: https://www.mdpi.com/2076-3417/11/3/1213

[20] "Council of europe contribution to the united nations 2030 agenda for sustainable development goals," https://www.coe.int/en/web/un-agenda-2030/home?desktop=true .

[21] B. Zhang and H. Zirath, "Metallic 3-D printed rectangular waveguides for millimeter-wave applications," *IEEE Transactions on Components, Packaging and Manufacturing Technology*, vol. 6, no. 5, pp. 796–804, 2016.

[22] A. Iliev, N. Kyurkchiev, and S. Markov, "On the approximation of the cut and step functions by logistic and gompertz functions," *BIOMATH*, vol. 4, 10 2015.

[23] A. J. Hanson and H. Ma, "Parallel transport approach to curve framing," Tech. Rep., 1995.

[24] Framing parametric curves. [Online]. Available: https://janakiev.com/blog/framing-parametric-curves/

[25] D. Carl, *The Parallel Transport Frame*, ser. Ed Game Programming Gems 2. Mark DeLouraCharles River Media, 2001.

[26] G. Toso and P. Angeletti, "An optimal procedure for the design of discrete constrained lens antennas with minimized optical aberrations. part i: Two-dimensional architectures," *Electronics*, vol. 11, no. 3, 2022. [Online]. Available: https://www.mdpi.com/2079-9292/11/3/493

[27] ——, "An optimal procedure for the design of discrete constrained lens antennas with minimized optical aberrations. part ii: Three-dimensional multifocal architectures," *Electronics*, vol. 11, no. 3, 2022. [Online]. Available: https://www.mdpi.com/2079-9292/11/3/503

[28] ——, "An optimal procedure for the design of discrete constrained lens antennas with minimized optical aberrations. part iii: Three-dimensional architectures with an extended field of view," *Electronics*, vol. 11, no. 5, 2022. [Online]. Available: https://www.mdpi.com/2079-9292/11/5/687

[29] C. Sciannella and G. Toso, "Imaging antenna systems with compensated optical aberrations based on unshaped surface reflectors," *International Patent US20160372835A1*, Publication Date: 22.09.2015 International Filing Date: 05.03.2014.

[30] ——, "An imaging reflector system with reduced scanning aberrations," *IEEE Transactions on Antennas and Propagation*, vol. 63, no. 4, pp. 1342–1350, 2015.

[31] D. McGrath, "Planar three-dimensional constrained lenses," *IEEE Transactions on Antennas and Propagation*, vol. 34, no. 1, pp. 46–50, 1986.

[32] V. Pascale, D. Maiarelli, L. D'Agristina, and N. Gatti, "Design and qualification of ku-band-radiating chains for receive active array antennas of flexible telecommunication satellites," *International Journal of Microwave and Wireless Technologies*, vol. 12, no. 6, p. 487–503, 2020.

Lisa Berretti (Member, *IEEE*) was born in Grosseto, Italy, in 1995. She received the B.Sc. and M.Sc. degree in Electronics Engineering in 2018 and 2020 from the University of Florence, Italy respectively. Since 2021 she is with the Institut d'Électronique et des Technologies du numéRiques (IETR), working at Institut National des Sciences Appliquées de Rennes (INSA Rennes), pursuing a Ph.D. degree. Her research interests include the conception of full-metallic discrete lenses and RF devices through additive manufacturing techniques and phase-only synthesis with genetic optimization techniques. Ms. Berretti was a recipient of some prizes, including the Ticra Travel Grant from the IEEE AP-S/URSI of 2019, Atlanta, GA, USA, and the Best Paper in the field of microwave theory and technique from the IEEE Microwave Theory and Techniques Society (MTT-S)/AP-S Chapter Central and Southern Italy.

This article has been accepted for publication in IEEE Transactions on Antennas and Propagation. This is the author's version which has not been fully edited and content may change prior to final publication. Citation information: DOI 10.1109/TAP.2023.3255515

Renaud Loison (Senior Member, *IEEE*) is professor at the Institut National des Sciences Appliquées (INSA), Rennes, France. He carries out his research activity at the Institut d'Électronique et des Technologies du numéRique (IETR) and mainly works on reflectarrays, metasurfaces and more generally on periodic and quasi-periodic surfaces.

Esteban Menargues (Senior Member, *IEEE*) Esteban Menargues was born in Alicante, Spain, in April 1986. He received the M.Sc. degree in electrical engineering from the Universidad Politécnica de Valencia, Valencia, Spain, in 2011. From 2011 to 2017, he was an RF Engineer with Aurorasat, Valencia, Spain; the Universidad Pública de Navarra, Pamplona, Spain; and the École Polytechnique Fédérale de Lausanne, Lausanne, Switzerland. In 2017, he joined SWISSto12 SA, Renens, Switzerland, as RF Engineer.

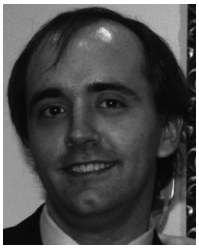

Santiago Capdevila (Senior Member, *IEEE*) was born in Barcelona, Spain. He received the M.Sc. and Ph.D. degrees in electrical engineering (with a minor in telecommunication engineering) from the Universitat Politécnica de Catalunya, Barcelona, in 2006 and 2013, respectively. In 2010, he joined the Department of Electrical and Computer Engineering, Henry Samueli School of Engineering, University of California at Irvine, Irvine, CA, USA, as a Visiting Scholar, under the FPU Fellowship Program. He was a Post-Doctoral Researcher with the Laboratory of Electromagnetics and Antennas, École Polytechnique Fédérale de Lausanne, Lausanne, Switzerland. He is currently a Senior RF Engineer with SWISSto12 SA, Renens, Switzerland.

Lucas Polo-López (Senior Member, *IEEE*) received the B.Sc., M.Sc. and Ph.D. degrees in Telecommunication Engineering in 2014, 2016 and 2020 from the Universidad Autónoma de Madrid (UAM), Madrid, Spain respectively. He began collaborating with the Radiofrequency Circuits, Antennas and Systems (RFCAS) group of this same university in 2014, while he was doing his B.Sc. thesis. Since 2021 he is with the Institut d'Electronique et des Technologies du numéRique (IETR), working at the Institut National des Sciences Appliquées de Rennes (INSA Rennes) as a post-doctoral fellow. His current research interests include the conception of novel antenna arrays and its modelling by means of hybrid simulation techniques, as well as the application of additive manufacturing techniques to the construction of antennas and waveguide devices. Dr. Polo-López has been recipient of two Best Ph.D. Thesis awards, one from COIT/AEIT and other from UAM, both in 2021 in Spain.

Giovanni Toso (S'93, M'00, SM '07, FM '23) received the Laurea Degree (cum laude), the Ph.D. and the Post Doctoral Fellowship from the University of Florence, Italy, in 1992, 1995 and 1999, respectively. During his PhD and Post Doc he spent more than one year as a Visiting Scientist at the Laboratoire d'Optique Electromagnetique de Marseille, France. In 1999, he was a Visiting Scientist with the University of California (UCLA) in Los Angeles. In 2000 received a scholarship from Alenia Spazio, Rome, Italy. In the same year he has been appointed Researcher at the Radio Astronomy Observatory of the Italian National Council of Research (CNR). Since 2000, he has been with the Antenna and Submillimeter Waves Section, European Space Agency (ESA), European Space Research and Technology Centre (ESTEC), Noordwijk, The Netherlands. He has been initiating several research and development activities on satellite antennas based on arrays, reflectarrays, discrete lenses, and reflectors. In particular, in the field of onboard satellite antennas, he has been coordinating activities on multibeam antennas (active and passive) mainly for Telecom applications. In the field of Terminal antennas, he has been supporting the development of reconfigurable antennas with electronic, mechanical, and hybrid scanning; some of these antennas are now available as products. He has promoted the development of the commercial software tool QUPES by TICRA, now used worldwide, for the analysis and design of periodic and quasi-periodic surfaces, such as reflectarrays, frequency selective surfaces, transmitarrays, and polarizers. Dr. Toso received, together with Prof. A. Skrivervik, the European School of Antennas (ESoA) Best Teacher Award in 2018. In 2014, he has been the Guest Editor, together with Dr. R. Mailloux, of the Special Issue on "Innovative Phased Array Antennas Based on Non-Regular Lattices and Overlapped Subarrays" published in the IEEE Transactions on Antennas and Propagation and, for the same society, has been an Associate Editor from 2013 to 2016. In 2018, he has been the Chairperson of the 39th ESA Antenna Workshop on "Multibeam and Reconfigurable Antennas". Since 2010, together with Dr. P. Angeletti, he has been instructing short courses on Multibeam Antennas and Beamforming Networks during international conferences, such as IEEE Antennas and Propagation Society (APS), IEEE MTT International Microwave Symposium (IMS), IEEE International Conference on Wireless Technology and Systems (ICWITS), European Conference on Antennas and Propagation (EuCAP), and European Microwave Week (EuMW), that have been attended by more than 1000 participants. Giovanni is the Organizer of the ESoA Course on Active Antennas. From January 2023 Giovanni Toso has been elevated to IEEE Fellow grade for contributions to multibeam antenna developments for satellite applications.

María García-Vigueras (Member, *IEEE*) was born in Murcia, Spain. She received the M.Sc. degree in telecommunications engineering and the Ph.D. degree from the Technical University of Cartagena, Cartagena, Spain, in 2007 and 2012, respectively.,From 2012 to 2015, she was a Research Fellow with the Laboratory of Electromagnetism and Antennas, École Polytechnique Fédérale de Lausanne, Lausanne, Switzerland. She is currently an Assistant Professor with the Institute National des Sciences Apliquées de Rennes, Rennes, France. She has coauthored more than 20 IEEE journals and 40 publications in international conferences. Her current research interests include leaky wave antennas, periodic surfaces, active antennas, waveguide feed chain components, and the evaluation of additive manufacturing's potential for RF design.,Dr. García Vigueras was a recipient of several prizes, including two Best Ph.D. Thesis Awards from COIT/AEIT in 2014 and UPTC in 2013, respectively, in Spain, and the Best Paper Awards in MAPE 2013 in Chengdu and EuCAP 2012 in Prague.